https://doi.org/10.5194/egusphere-2026-5861
Preprint. Discussion started: 2 November 2026
© Author(s) 2026. CC BY 4.0 License.

Age-dependence of fracture toughness and microstructure in saline ice

Sid Oksala[1], Sakshi Devi[1], Waqas Ahmad[2], Jukka Kuva[3], and Jukka Tuhkuri[1]

[1]Department of Energy and Mechanical Engineering, Aalto University, Espoo, Finland
[2]Trueflaw, Espoo, Finland
[3]Geological Survey of Finland, Espoo, Finland

Correspondence: Sid Oksala (sid.oksala@aalto.fi)

Abstract. The mechanical behaviour of sea ice evolves substantially as the ice ages, yet the mechanisms governing the associated changes in fracture resistance remain poorly understood. Here, we investigate the ageing of columnar saline ice through a multi-scale experimental fracture campaign combining controlled laboratory ageing, Arctic field measurements, and three-dimensional X-ray micro-computed tomography (μCT). Laboratory-grown ice exhibits a pronounced increase in fracture toughness (K_{IC}) over 120 days of ageing, accompanied by an increase and eventual plateau in the work required. The fracture toughness of aged natural sea ice follows the established inverse relationship with the square root of brine volume, whereas the fracture behaviour of younger laboratory ice cannot be explained by brine volume alone. Instead, μCT observations reveal microstructural evolution: dispersed brine inclusions coalesce into increasingly interconnected drainage channels with larger apertures, altering the geometry and spatial distribution of internal flaws. These observations suggest that this structural consolidation reduces local stress concentrations and forces crack propagation to transition from a highly splintered path to a singular, energy-intensive fracture, providing a physical explanation for the observed toughening. Together, these results demonstrate that ice age is a powerful predictive parameter for evaluating fracture resistance, while highlighting microstructural evolution as a fundamental physical mechanism driving this temporal toughening.

1 Introduction

The physical properties of sea ice change as the material ages. This has been a pillar of knowledge for indigenous Arctic communities long before the formalization of ice mechanics as a scientific discipline. Early polar explorers, such as Fridtjof Nansen, documented this knowledge, for example noting that while young sea ice is too saline for consumption, older ice undergoes a natural desalination process that eventually provides a reliable source of fresh water (Nansen and Sverdrup, 1897). Modern research has since formalised these observations, showing that as sea ice ages, continuous developments in its salinity, temperature, density, and microstructure dictate its material behaviour (Weeks, 2010; Schulson and Duval, 2009). Because the large-scale failure of the ice cover is fundamentally driven by crack propagation (Dempsey, 1991), understanding how this ageing affects the material's fracture processes is critical.

To evaluate these processes, linear elastic fracture mechanics (LEFM)—while subject to caveats when applied to saline ice—provides a framework for evaluating brittle failure in ice sheets. Because ice at high homologous temperatures is vis-

https://doi.org/10.5194/egusphere-2026-5861
Preprint. Discussion started: 2 November 2026
© Author(s) 2026. CC BY 4.0 License.

coelastic, crack-tip creep and process zone development can introduce specimen-size dependencies (Dempsey, 1991; Dempsey et al., 1999; Cole, 2001). Despite these limitations, under rapid loading rates or localized stress concentrations, ice behaves primarily as a brittle solid where fracture processes dominate over ductile creep. In these regimes, the critical stress-intensity factor (K_{IC}) provides a practical parameter for predicting the unstable propagation of preexisting flaws and starter cracks (Dempsey et al., 1999; Rist et al., 1996). Furthermore, LEFM remains the standard approach because it enables comparability with historical literature and provides a means to normalize load values by specimen size and geometry. Consequently, quantifying K_{IC} provides a basis for assessing large-scale edge cracking, crevasse penetration, and ice-structure contact mechanics (Smith, 1976; Timco and Frederking, 1983; Rist et al., 1996).

Historically, quantifying this evolving fracture behaviour has relied on isolating specific physical parameters. Because variables such as temperature, salinity, and porosity change continuously from the surface to the ice-water interface, the fracture toughness (K_{IC}) of the ice cover exhibits a pronounced depth-dependent variation. For example, both Rist et al. (1996) and Timco and Frederking (1983) demonstrated that fracture toughness generally increases downward as the ice transitions from a porous surface layer into a denser interior. However, they also noted that sharp drops in resistance can occur at deeper boundaries due to localized shifts in crystal morphology, grain size, and impurity distribution. Furthermore, Timco and Frederking (1983) explicitly linked this strong vertical profile in seasonal sea ice directly to continuous variations in salinity and brine volume.

Beyond this vertical heterogeneity, fracture resistance is governed by a complex interplay of material, geometric, and temporal factors. Recent work continues to link toughness to diverse physical parameters, such as thickness-independence in columnar freshwater ice (Gharamti et al., 2024) and melt-induced density shifts in glacial ice (Pearce et al., 2025). Spatially, fracture toughness is heavily influenced by the structural scale of the ice; while local resistance is dictated by temperature and salinity gradients (Dempsey et al., 2018), large-scale field tests (up to $L = 80$ m) demonstrate a pronounced scale effect where K_{IC} increases with specimen size before plateauing (Dempsey et al., 1999). Temporally, historical data from Barrow, Alaska, suggest a seasonal evolution, with fracture toughness doubling between November and March (Adamson et al., 1997; LeClair et al., 1997). However, direct comparisons across these studies remain difficult because the experiments were performed under disparate environmental conditions, varying c-axis alignments, and temperature fluctuations.

Furthermore, a disparity persists between measurements taken from large-scale field tests and small-scale laboratory experiments. This variance has traditionally been explained by the scale effect, driven by the fracture process zone (FPZ) in ice, which small specimens were thought to be unable to fully accommodate (Dempsey, 1991). While this effect is well-documented, recent findings by Ahmad (2024) suggest that the FPZ may be limited to the millimetre scale. This implies that laboratory-scale specimens should, in theory, be sufficient to capture intrinsic material behaviour, yet the gap between laboratory- and field-measured values remains poorly understood.

At the microstructural level, it is known that internal flaws, grain boundaries, and brine pockets govern ice deformation by acting as localized stress concentrations that trigger crack nucleation (Cole, 2001). Cole and Shapiro (1998) demonstrated that first-year sea ice brine networks consolidate into open vertical pathways or freeze shut depending on seasonal thermal states, directly altering macroscopic failure paths. Using X-ray micro-computed tomography (μCT) analysis, Lieb-Lappen

https://doi.org/10.5194/egusphere-2026-5861
Preprint. Discussion started: 2 November 2026
© Author(s) 2026. CC BY 4.0 License.

et al. (2018) further proved that ice crystal fabric dictates this topology; columnar ice forms straight, vertically aligned channels with large throat sizes and higher connectivity. Building on these structural observations, Oksala et al. (2026) recently utilized μCT to directly link these microstructural features to the physical propagation paths of tensile fractures. Despite these advances, structural characterizations have predominantly focused on naturally formed ice at discrete points in time; none have monitored the continuous temporal evolution of the same parent ice sheet to isolate ageing effects from geographic or structural variability.

This study presents a multi-phase, multi-scale experimental campaign designed to isolate the effects of ageing from environmental and geographic variability. By maintaining laboratory-grown parent ice sheets under controlled conditions for several months, we continuously harvested and tested specimens as the material aged. We conducted small-scale ($R = 70$ mm) and medium-scale ($R = 150$ mm) semi-circular bend (SCB) tests (Kuruppu et al., 2014) alongside large-scale edge-cracked rectangular plate (ECRP) tests ($L = 750$ mm) to capture this age-dependent behaviour across an order of magnitude in size. These experiments are combined with μCT scans taken along crack paths to examine how the evolution of the microstructure affects crack propagation. Finally, these controlled laboratory findings are validated against natural field data collected in Svalbard, providing insight into the Mode-I fracture behaviour of saline ice as it ages.

2 Experimental Methods

Four experimental campaigns were conducted to evaluate the effect of physical parameters on the fracture properties of ageing S2 saline ice—characterized by a random c-axis orientation within the horizontal plane (Weeks, 2010). The research was divided into two primary laboratory studies conducted in the Aalto University cold room in Espoo, Finland and two field validation campaigns in Van Mijenfjorden, Svalbard. The first laboratory campaign (Summer 2024) utilized medium-scale SCB specimens ($R \approx 150$ mm) tested under displacement control. The second laboratory campaign (Summer 2025) utilized small-scale SCB specimens ($R \approx 70$ mm) tested under load control and large-scale *in situ* ECRP specimens (1500×750 mm) tested under displacement control. In both laboratory settings, the ice was grown within a temperature- and salinity-controlled environment as specified by Oksala et al. (2024) and aged *in situ*. Schematic diagrams of the specimen geometry can be seen in Fig. 1.

These laboratory experiments were benchmarked against small scale SCB experiments conducted on sea ice in the Van Mijenfjorden, Svalbard (March 2025 and March 2026). All experiments were conducted as Mode I fracture tests, with the crack front oriented parallel to the columnar grains. ECRP testing used the device described by Ahmad (2024), and SCB experiments and all data collection were performed according to Oksala et al. (2025). A summary of these four experimental phases, is provided in Table 1. A comprehensive dataset for all experimental campaigns is provided in the Supplementary Material, and the raw data are accessible as detailed in the Data Availability statement.

2.1 Phase I: Medium-scale laboratory SCB experiments (Aalto University 2024)

SCB specimens were grown in 300 mm diameter High-Density Polyethylene (HDPE) moulds floating in an ice growth basin within a cold room. To accurately mimic the thermodynamic conditions of natural sea ice, the specimens were grown and

https://doi.org/10.5194/egusphere-2026-5861
Preprint. Discussion started: 2 November 2026
© Author(s) 2026. CC BY 4.0 License.

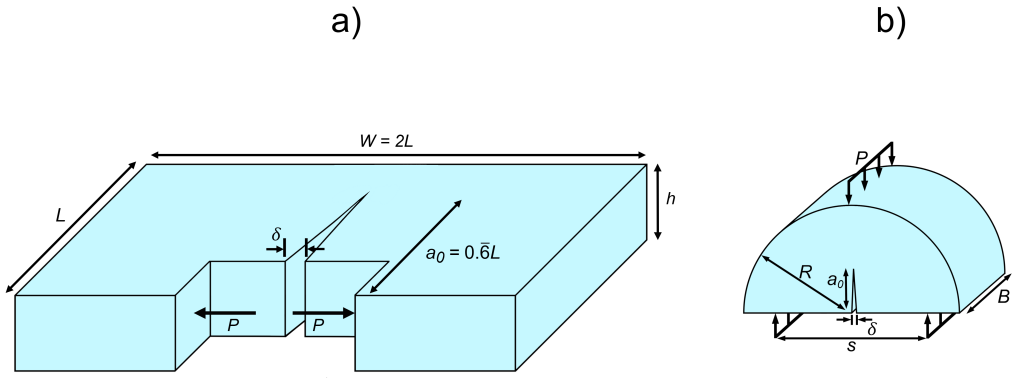


Figure 1. Schematic representation of the test geometries: a) the ECRP specimen showing applied force P, crack mouth opening displacement (CMOD) δ, specimen width W, length L, thickness h, and initial notch length a_0; b) the SCB specimen illustrating the span length s, initial notch length a_0, specimen radius R, applied force P, and thickness B.

Table 1. Chronological summary of experimental phases I–IV. Geometry refers to SCB and ECRP specimens. Size refers to radius (R) for SCB and length parallel to the crack (L) for ECRP specimen. Testing modes include displacement control (DC) and load control (LC) protocols, with typical test duration in minutes. Laboratory ice was grown from a 34 ppt NaCl solution; natural sea ice was tested on-site. n is the number of specimen tested

Ice Type	Geometry	Size (mm)	Mode (Duration)	Age (days)	n
Phase I (Lab): Summer 2024; Cold Room, Aalto University, Finland					
Lab-grown S2 Ice	Med. SCB	150	DC ($\approx$ 30 min)	14–62	24
Phase II (Field): Mar. 2025; Van Mijenfjorden, Svalbard					
First-year sea ice	Sml. SCB	70	LC ($<$ 1 min)	$\approx$ 100*	16
Phase III (Lab): Summer 2025; Cold Room, Aalto University, Finland					
Lab-grown S2 Ice	Sml. SCB	70	LC ($<$ 1 min)	26–119	63
Lab-grown S2 Ice	Lrg. ECRP	750	DC ($\approx$ 45 min)	26–119	4
Phase IV (Field): Mar. 2026; Van Mijenfjorden, Svalbard					
First-year sea ice	Sml. SCB	70	LC ($<$ 1 min)	$\approx$ 120*	8

*Estimated age based on ice charts provided by the **?**.

https://doi.org/10.5194/egusphere-2026-5861
Preprint. Discussion started: 2 November 2026
© Author(s) 2026. CC BY 4.0 License.

maintained in a strictly temperature- and salinity-controlled environment (Oksala et al., 2024). This environmental control, combined with the density of the HDPE which allowed the samples to float in equilibrium during freezing, actively promoted natural brine drainage and ageing processes. To ensure a columnar S2 structure, the ice sheet was seeded by spraying a fresh-
95 water mist into the air once the solution reached 0°C. The ice sheet was aged for 62 days at a stable air temperature of -12.5°C, during which the bulk salinity decreased from 7.5 ppt to 4.3 ppt. The resulting columnar grain structure was verified through horizontal and vertical thin sections.

Every two weeks, 2 to 6 moulds were removed from the parent ice sheet; the top 100 mm was processed into SCB specimens with a radius $R \approx 150$ mm and thickness $B \approx 100$ mm (Fig. 1b). An initial notch of length $a_0 \approx 70$ mm was cut into each
100 specimen using a handsaw and sharpened using a razor blade. All experiments were performed under displacement control such that the crack mouth opening displacement (CMOD) was increased at a constant, relatively slow, rate of 1 μm/s, resulting in total test durations of approximately 30 minutes. The tests were conducted using a span length $s = 212$ mm.

While recognizing that process zone development and viscoelasticity complicate the strict application of LEFM in sea ice, normalizing experimental loads into K_{IC} values remains an effective method to account for specimen geometry and facilitate
105 comparison with historical data. Accordingly, the fracture toughness for the SCB geometries was calculated using the method proposed by Kuruppu et al. (2014):

$$K_{IC} = \frac{P_p \sqrt{\pi a_0}}{2RB} Y'(s/R, \beta) \tag{1}$$

where P_p is the peak load, a_0 is the initial notch length, and Y' is the dimensionless stress intensity factor. Although recent investigations suggest that evaluating K_{IC} using true crack initiation loads or propagated crack lengths yields a more precise
110 representation of fracture behaviour (Ahmad, 2024), isolating these parameters experimentally remains challenging. Therefore, this study adopts the traditional formulation relying on peak load and initial notch length, which provides a conservative, lower-bound estimate of the fracture toughness.

2.2 Phase II: Small-scale field SCB experiments (Svalbard 2025)

While Van Mijenfjorden experienced varying degrees of drift ice as early as November 11th of the previous year, stable fast
115 ice formation was established by January 23rd (**?**). Consequently, at the time of testing on March 25th, the estimated age of the ice ranged between 61 and 134 days. Subsequent analyses treat these specimens as being 98 days old, representing the mean.

To obtain the samples, two vertical cores were extracted from the ice sheet using a 140 mm Kovacs Mark V coring system. These cores were rapidly sectioned and halved into SCB geometries (thickness $B \approx 100$ mm) to preserve in-situ temperatures. An initial notch $a_0 \approx 40$ mm was cut into each specimen using a handsaw and sharpened with a razor blade. The experiments
120 utilized load control (10 N/s), resulting in test durations of less than 1 minute. The support span was fixed at $s = 104$ mm. Fracture toughness (K_{IC}) was calculated using Equation 1 as in Phase I (Lab).

Vertical profiles of salinity, temperature, and density were collected at 50 mm intervals. The ice sheet was characterized by temperatures between -5.5°C and -2.8°C, salinity values ranging from 4 to 9.5 ppt, and densities between 880 and 930 kg/m^3. Additionally, the grain structure was verified through thin-section analysis. To estimate the brine volume fraction

https://doi.org/10.5194/egusphere-2026-5861
Preprint. Discussion started: 2 November 2026
© Author(s) 2026. CC BY 4.0 License.

(ν_b), we utilized the established formulation by Frankenstein and Garner (1967), which relies on bulk salinity and temperature:

$$\nu_b = S\left(\frac{45.917}{|T|} + 0.930\right) \times 10^{-3}, \tag{2}$$

where S is the bulk salinity in ppt, and T is the temperature in °C.

2.3 Phase III: Multi-scale laboratory SCB and ECRP experiments (Aalto University 2025)

A 2×4 m^2 parent ice sheet was grown in an ice basin within a cold room. As in the previous laboratory phase, the ice was subjected to a temperature- and salinity-controlled environment (Oksala et al., 2024) specifically designed to promote natural thermodynamic ageing over the duration of the campaign. The sheet was seeded by spraying a freshwater mist into the air once the solution reached 0°C to ensure a columnar S2 structure. The sheet was aged at an air temperature between -10 and -5°C, reaching a thickness of approximately 300 mm by day 26 and maintained at this thickness for the remainder of the 120-day campaign. Throughout this controlled ageing process, the bulk salinity of the ice sheet decreased from 6.0 ppt to 3.9 ppt. During each set of experiments, the vertical temperature and salinity profiles of the ice were measured. The resulting columnar grain structure was verified through horizontal and vertical thin sections.

Small-scale SCB specimens were prepared from cores extracted from the ice sheet using the previously described coring system. Each core was sliced into 60 mm thick sections and halved, yielding up to 10 specimens per core. An initial notch $a_0 \approx 35$ mm was cut and sharpened as before. The experiments were conducted under load control at a rate of 10 N/s. The fracture toughness K_{IC} was calculated using Equation 1 as in previous phases. The brine volume of each SCB specimen was estimated using Equation 2.

Large-scale ECRP experiments were conducted on the full-thickness ice sheet. These specimens had $W = 1500$ mm and $L = 750$ mm with an initial notch $a_0 = 500$ mm (Fig. 1a). Specimen thickness was $h \approx 300$ mm. These experiments were performed under displacement control such that the CMOD was increased at a slow rate of 1 μm/s, resulting in test durations of approximately 45 minutes. The tests were terminated when the loading device reached its maximum stroke capacity, prior to complete specimen failure.

Fracture toughness was calculated with peak load P_p and initial notch length a_0 using the weight function methodology developed by Dempsey and Mu (2014):

$$K_{IC} = \frac{P_p}{Dh}\sqrt{\frac{2a_0}{\pi}}\, Z_1(D, a_0, L) \tag{3}$$

where D is the loading contact length (100 mm), and Z_1 is a dimensionless geometric factor. Alongside fracture toughness, the work (W) was calculated to characterize the total energy dissipated during testing. Standard energy-based fracture metrics, such as the J-integral or the size-normalised work of fracture, require precise knowledge of the crack initiation point or the total propagated crack area, respectively. Because estimating crack initiation directly from force-CMOD data is difficult (Ahmad, 2024; Devi et al., 2026), and our large-scale experiments were terminated prior to complete specimen failure (meaning the propagated crack length cannot be approximated as the initial uncracked ligament), these standard metrics could not be reliably

https://doi.org/10.5194/egusphere-2026-5861
Preprint. Discussion started: 2 November 2026
© Author(s) 2026. CC BY 4.0 License.

evaluated. Instead, we utilize work, determined by calculating the area under the load-displacement curve up to a CMOD of 0.0025 m, selected because it was the maximum displacement consistently achieved across all tests prior to termination:

$$W = \int_0^{0.0025} P(\delta)\, d\delta \tag{4}$$

where $P(\delta)$ is the applied load integrated with respect to the crack mouth opening displacement δ.

To investigate the microstructural evolution of the ageing ice, cylindrical samples were extracted from along the crack path of the ECRP specimens at 55 and 119 days for µCT scanning. These samples, measuring approximately 40 mm in both diameter and height, were scanned at the Geological Survey of Finland using a GE phoenix v|tome|x s system equipped with a Deben CT5000 TEC environment chamber. To maintain the temperature of the samples during scanning, the Deben stage Peltier elements were set to $-10\,^{\circ}\mathrm{C}$ for the duration of the scan. The scans were conducted with an accelerating voltage of 45 kV and tube current of 625 μA for a total power of 28.125 W, yielding a voxel size of 25 μm. No beam filter was used. During a 360° rotation, 2700 projections were taken where at each angle the detector waited for a single exposure time and then took an average of three exposures. With a single exposure time of 500 ms, the total scan time was 90 minutes. Beam hardening correction, which is a dimensionless number between 0 and 10, was set to 6 and no ring artefact reduction was used. The three components present in the ice (air, salt water, and solid ice) were segmented and analysed using ThermoFisher PerGeos 2020.2 and a marker-based watershed tool. Statistics on the microstructure were obtained using the BoneJ plugin (Domander et al., 2021) in FIJI/ImageJ.

Subsequent morphological analysis of the crack, identified as the primary connected void networks, was performed using MATLAB. The normalised surface area (A_N) was calculated by estimating the true surface area of the crack and dividing it by twice the nominal projected area. To quantify whether the crack propagated as a single complex feature or splintered into parallel overlapping planes—as observed by Oksala et al. (2026)—we introduce a novel metric termed the Mean Parallel Fronts (MPF). Designed to capture the degree of crack splintering, the MPF is determined by extracting cross-sections—in this case, 50 slices—perpendicular to the overall crack propagation direction, spaced evenly along its length. Within each 2D cross-section, the number of discrete, disconnected crack fronts is counted. Averaging these across all slices yields the MPF, providing a direct numerical representation of how heavily the fracture front splintered as it navigated the microstructure.

2.4 Phase IV: Small-scale field SCB experiments (Svalbard 2026)

The final experimental campaign was conducted in Vallunden, a semi-enclosed lagoon connected to Van Mijenfjorden, Svalbard. Estimating the ice age at the time of testing on March 24th requires consideration of both regional ice conditions and local topography. The estimated age of the ice ranges between 96 days (stable regional fast ice formation) and 144 days (earliest regional drift ice observations) (**?**). Subsequent analyses treat these specimens as 120 days old, representing the mean of this time frame, consistent with Phase II (Field).

Cylindrical cores were extracted as before and prepared into SCB specimens ($B \approx 60$ mm). Each specimen was notched to a depth of $a_0 \approx 35$ mm and tested under load control at 10 N/s, ensuring consistency with the previous experimental phases.

https://doi.org/10.5194/egusphere-2026-5861
Preprint. Discussion started: 2 November 2026
© Author(s) 2026. CC BY 4.0 License.

The fracture toughness K_{IC} was calculated using Equation 1 as in previous phases. Vertical profiles of salinity, temperature, and density were collected at ≈ 60 mm intervals. The tested ice sheet was characterized by temperatures between -4.4 and -2.3°C, salinity values ranging from 4.7 to 8.9 ppt, and densities of 880–921 kg/m^3. Brine volume ν_b for the tested specimens was estimated using Equation 2.

3 Results

The following results characterize the fracture behaviour of saline ice as it ages across varied scales, geometries, and loading modes. Fracture properties are presented alongside corresponding environmental data. A global summary of the age-dependent strengthening trend is presented first, followed by a detailed analysis of the specific mechanical responses in order of decreasing spatial scale (from large-scale ECRP to small-scale SCB specimens). Finally, the physical parameters driving this strengthening process—specifically temperature, salinity, density, and microstructure—are discussed.

3.1 Ageing trend

The evolution of fracture toughness and work with age across the three specimen scales and two geometries is summarized in Fig. 2. Irrespective of specimen geometry or scale, the ice exhibits a pronounced age-dependent strengthening. In the large-scale ECRP experiments, K_{IC} steadily climbs over the ageing period, reaching approximately 90 kPa$\sqrt{\text{m}}$ by day 119. This strengthening is corroborated by the work (W) of the ECRP specimens, which doubles from 1.43 J at 26 days to a peak of 2.98 J at 84 days, before plateauing at 2.81 J by day 119. For the medium-scale SCB specimens, an increase in mean fracture toughness occurs during the early ageing phase, climbing from 29.0 kPa$\sqrt{\text{m}}$ at day 14 to a peak value of nearly 70 kPa$\sqrt{\text{m}}$ at day 43. Beyond 43 days, a reduction in K_{IC} is observed, settling at approximately 51 kPa$\sqrt{\text{m}}$ by day 62—a variation that falls well within the scatter of the overall strengthening trend. Finally, in the small-scale SCB tests, the peak fracture toughness (calculated as the mean of the highest values extracted from each core of a given age) demonstrates a consistent upward trend in both laboratory and field conditions. The laboratory samples increase from approximately 49 kPa$\sqrt{\text{m}}$ at 27 days to 82 kPa$\sqrt{\text{m}}$ by 120 days, a trajectory matched by the field samples, which reach 83 kPa$\sqrt{\text{m}}$ by day 120. While these early-age toughness values are relatively low, the results for the aged ice are in agreement with established literature on natural saline ice (Schulson and Duval, 2009). Comprehensive experimental parameters across all phases are summarized in Table 2.

Force–displacement analysis is restricted to the large ECRP and medium SCB specimens (Fig. 3), as these were conducted under displacement control, unlike the load-controlled small-scale SCB experiments. Peak force has been identified for all test cases. A qualitative inspection of the ECRP data (Fig. 3) reveals a increasing trend in both peak force—rising from 772 N at 26 days to 1572 N at 118 days—and material stiffness. To isolate intrinsic material strengthening from geometric artifacts caused by fluctuating specimen thickness (h), peak loads were normalised (P_p/h) in accordance with Gharamti et al. (2024). Even after this normalisation, the strength shows a distinct increasing trend—rising from 2.76 kN/m to 4.52 kN/m between 26 and 84 days, before appearing to plateau between 84 and 119 days. Consequently, while the raw force data is plotted to maintain an intuitive physical scale, the pronounced strengthening of the ice over the campaign is demonstrably driven by the

https://doi.org/10.5194/egusphere-2026-5861
Preprint. Discussion started: 2 November 2026
© Author(s) 2026. CC BY 4.0 License.

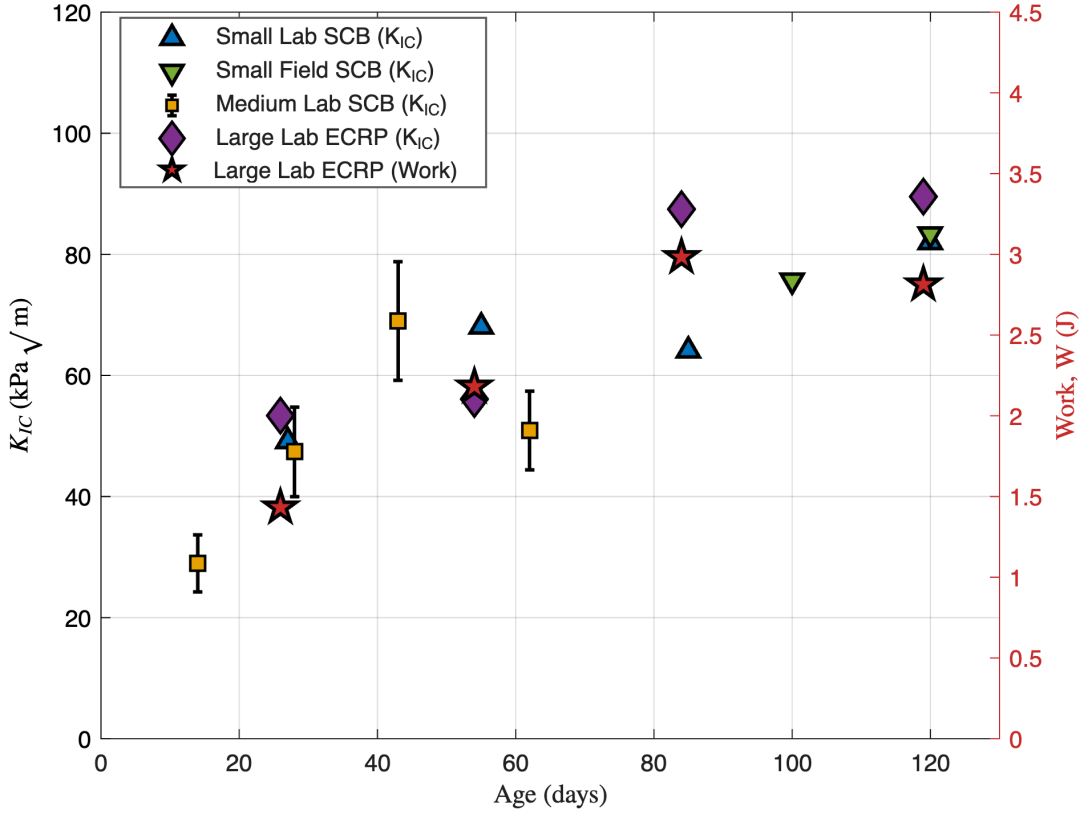


Figure 2. Evolution of fracture toughness (K_{IC}) and work (W) with ice age across different specimen scales and environments. The plot compares mean values (± standard deviation) for medium-scale laboratory SCB specimens (Phase I), peak values for small-scale laboratory and field SCB specimens (Phases II, III, and IV), and discrete values for large-scale laboratory ECRP specimens (Phase III).

ageing process itself, independent of specimen thickness. Despite the differences in testing configuration and scale, both the ECRP and SCB specimens (Fig. 3) exhibit a consistent mechanical response characterized by a sustained, relatively constant force over extended CMOD values. This shared behaviour demonstrates that variations in specimen scale and geometry do not fundamentally alter the underlying fracture processes.

For the small SCB specimens, it is a significant challenge to directly relate their depth-dependent fracture properties to the global fracture behaviour observed in the full-thickness ECRP tests. Applying a uniform mean across the entire vertical profile of an ice core risks assigning an unrealistically high statistical weight to the structurally weak skeletal layer at the ice–water interface, which likely contributes minimally to the fracture toughness of the full ice sheet. To properly account for this heterogeneity, the small-scale data are instead characterized by evaluating the minimum, mean, and maximum fracture toughness (K_{IC}) values extracted from each core. The minimum and maximum values are calculated as the mean of the lowest and highest values extracted from each core of a given age, respectively. Because only two to three cores were evaluated at each age, standard deviations for these extremes have not been calculated. By analysing the laboratory SCB (Phase III) data via these

https://doi.org/10.5194/egusphere-2026-5861
Preprint. Discussion started: 2 November 2026
© Author(s) 2026. CC BY 4.0 License.

Table 2. Summary of experimental fracture results for all test phases. Sections (a) and (b) summarize the medium-scale (Phase I) and small-scale (Phases II, III, and IV) SCB specimens, comparing laboratory-grown and natural sea ice. Section (c) presents the fracture results across the four Phase III ECRP specimens. Here, δ denotes the CMOD, P_p is force, h is thickness, K_{IC} is the Mode I fracture toughness, and W is work calculated up to a CMOD of 0.0025 m. n denotes number of samples.

(a) Phase I (Lab) Medium-Scale SCB

Age (d)	mean K_{IC} (kPa $\sqrt{\text{m}}$)	Std. Dev.	n
14	29.0	4.7	6
28	47.4	7.4	9
43	69.0	9.8	4
62	50.9	6.5	5

(b) Phase II, III and IV Small-Scale SCB

Specimen Series	Age (d)	Min	mean K_{IC} (kPa $\sqrt{\text{m}}$)	Std. Dev.	Max	n
Phase III (Lab)	27	33.2	41.2	9.1	49.1	6
	55	14.4	40.6	18.9	68.1	16
	85	17.2	44.2	17.5	64.1	20
	120	38.4	55.3	14.4	82.0	21
Phase II (Field)	≈100	30.25	58.5	19.3	75.7	16
Phase IV (Field)	≈120	19.4	58.0	22.3	83.3	8

(c) Phase III (Lab) Large-Scale ECRP

Age (d)	δ_p (μm)	P_p (N)	h (m)	P_p/h (kN/m)	K_{IC} (kPa$\sqrt{\text{m}}$)	W (J)
26	446	772	0.28	2.76	53.4	1.43
54	244	928	0.32	2.90	56.1	2.18
84	229	1311	0.29	4.52	87.5	2.98
118	707	1572	0.34	4.62	89.5	2.81

https://doi.org/10.5194/egusphere-2026-5861
Preprint. Discussion started: 2 November 2026
© Author(s) 2026. CC BY 4.0 License.

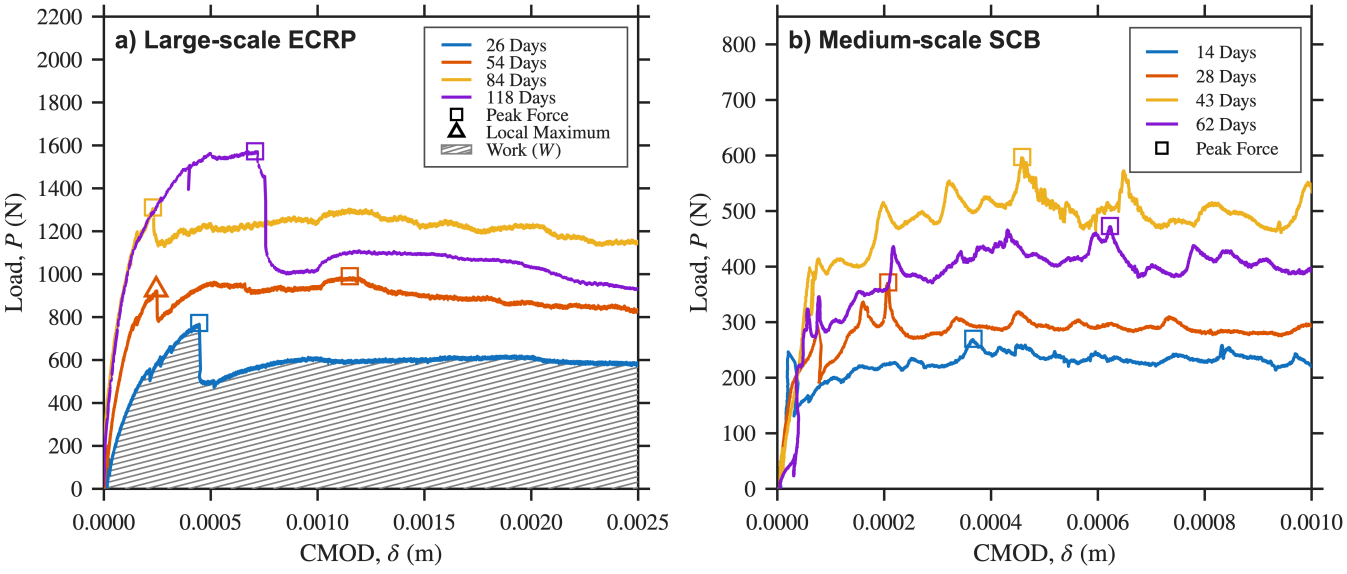


Figure 3. Representative force–displacement (load–CMOD) curves for the displacement-controlled experiments. (a) Phase III (Lab) large-scale ECRP specimens across four ageing stages (26 to 118 days). The hatched area under the 26-day curve illustrates the work (W) integrated up to a CMOD of 0.0025 m. For the 54-day sample, calculations utilize the local maximum (△), as the peak occurred at an unrepresentative displacement. (b) Phase I (Lab) medium-scale SCB specimens across four ageing stages (14 to 62 days). Across both panels, square markers (□) denote the peak force.

values (Table 2), distinct trends emerge. The minimum recorded fracture toughness values exhibit no clear increasing trend with age, fluctuating between 14.4 and 38.4 kPa$\sqrt{\text{m}}$. This suggests that the skeletal layer of the ice remains relatively weak regardless of the overall growth duration. The mean K_{IC} exhibits only a mild dependence on age, rising from 41.2 ± 9.1 kPa$\sqrt{\text{m}}$ at 27 days to 55.3 ± 14.4 kPa$\sqrt{\text{m}}$ at 120 days. In contrast, the maximum K_{IC} values demonstrate a strong dependence on age, increasing from 49.1 kPa$\sqrt{\text{m}}$ at 27 days to 82.0 kPa$\sqrt{\text{m}}$ at 120 days. This increase in the maximum values—plotted as the peak fracture toughness in Fig. 2—aligns well with the trends observed at the larger scales.

Across both field campaigns, the natural ice exhibited highly consistent mean fracture toughness (K_{IC}) values of 58.5 ± 19.3 kPa$\sqrt{\text{m}}$ (Phase II (Field)) and 58.0 ± 22.3 kPa$\sqrt{\text{m}}$ (Phase IV (Field)). The significant variance observed within these datasets is attributed to the vertical heterogeneity of the ice cover. Because the specimens were tested at discrete depths through the entire thickness of the ice sheet, the data inherently capture the vertical gradients in temperature, salinity, density, and grain structure. This depth dependence is reflected in the wide range between the peak values (75.7 and 83.3 kPa$\sqrt{\text{m}}$ for Phases II (Field) and IV (Field), respectively) and the minimum values (19.4 and 30.25 kPa$\sqrt{\text{m}}$, respectively), mirroring the vertical heterogeneity observed in the laboratory experiments. Notably, both the mean and peak toughness values from the natural field campaigns show excellent agreement with the 120-day laboratory specimens. This strong correlation demonstrates that the laboratory-grown ice reaches a fracture resistance comparable to natural sea ice, validating the ageing methodologies employed in this study.

https://doi.org/10.5194/egusphere-2026-5861
Preprint. Discussion started: 2 November 2026
© Author(s) 2026. CC BY 4.0 License.

The depth profile (Fig. 4) reveals a distinct and consistent vertical variance across both field campaigns: the ice exhibits moderate fracture resistance at the top surface, reaches maximum strength within the solid mid-section (approximately 15 to 35 cm in depth), and weakens significantly at the bottom (this trend was mirrored in the thinner laboratory ice, though omitted here to prevent scale distortion). The fact that the peak small-scale values align so closely with the full-thickness ECRP results suggests that fracture resistance is localized. Rather than acting as a uniform material, the ice sheet's overall toughness is dominated by its structurally robust mid-section, while the porous skeletal layer provides negligible resistance.

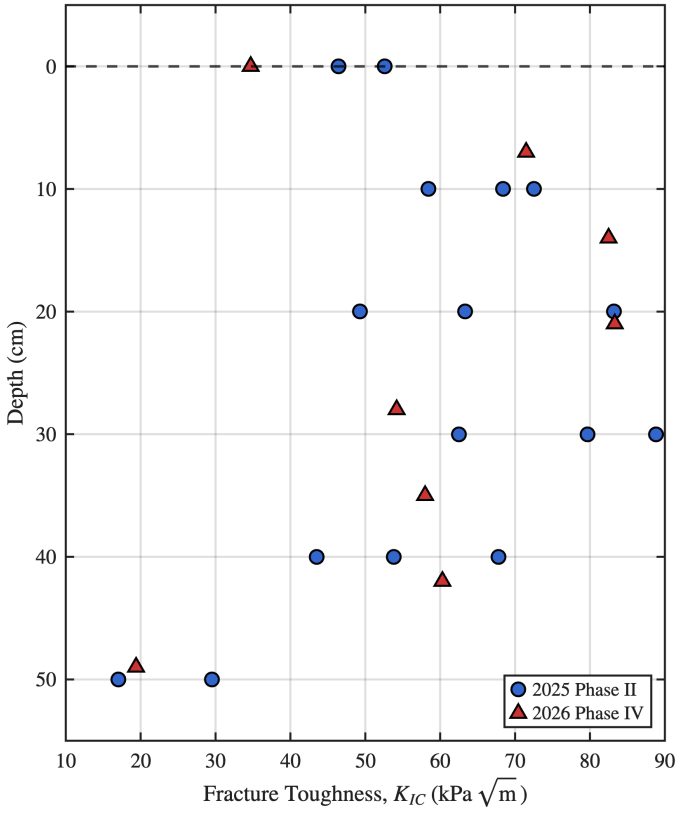


Figure 4. Depth profile of Mode I fracture toughness (K_{IC}) for the natural sea ice evaluated during Phase II (2025 field experiments) and Phase IV (2026 field experiments). The data demonstrate a vertical variance, characterized by moderate strength at the surface, a fracture-resistant mid-section, and a structurally weak skeletal layer at the ice–water interface.

3.2 Physical Parameters

While age serves as a convenient classifier for the ice cover, it is not a physical property. Typically, the mechanical behaviour of sea ice is argued to be governed by its macroscopic variables—specifically temperature, salinity, and density. However, it has been demonstrated that the internal microstructure plays a significant role as well. Consequently, it is critical to determine whether the age-dependent increase in fracture toughness observed in this study is solely an effect of evolving thermodynamic

https://doi.org/10.5194/egusphere-2026-5861
Preprint. Discussion started: 2 November 2026
© Author(s) 2026. CC BY 4.0 License.



variables, or if it is also driven by microstructural transformations. To investigate this, we first utilize the mid season natural sea ice data to establish baseline macroscopic trends. Analysis of this field data confirms that fracture resistance is governed by the coupled interaction of these variables; attempting to correlate K_{IC} against any single parameter yields scattered distributions with weak to no discernible trend. It is only when these properties are contextualized together—such as evaluating density or salinity within specific thermal regimes—that clear physical relationships emerge against which the laboratory ice can be benchmarked.

As shown in Fig. 5a, evaluating the density data within a consistent thermal regime (e.g., $-5.5°\text{C} \leq T < -4.0°\text{C}$) demonstrates that K_{IC} increases from approximately 30 to 90 kPa$\sqrt{\text{m}}$ as the density rises from 880 to 920 kg m^{-3}. Furthermore, the effect of temperature is evident when observing specimens at a constant density; at a density of approximately 915 kg m^{-3}, warmer specimens yield significantly lower fracture toughness (falling below 30 kPa$\sqrt{\text{m}}$) compared to their colder counterparts (which exceed 80 kPa$\sqrt{\text{m}}$). A parallel coupled effect is observed in the salinity data (Fig. 5b). When partitioned by temperature, distinct inverse trends emerge, demonstrating that higher salinity generally yields lower fracture toughness. Yet, as observed with the density data, temperature exerts a strong independent influence. At any given constant salinity, warmer ice exhibits a lower fracture toughness compared to its colder counterparts. Notably, small variations in density ($\Delta\rho \approx 40$ kg m^{-3}) and temperature ($\Delta T \approx 3.0°\text{C}$) result in relatively large variations in fracture toughness ($\Delta K_{IC} \approx 60$ kPa$\sqrt{\text{m}}$).

While temperature, salinity, and bulk density individually correlate with fracture resistance, they are not independent variables. Together, they dictate the liquid brine volume fraction, which physically represents the network of internal flaws. Plotting the fracture toughness (K_{IC}) against the square root of the brine volume ($\sqrt{\nu_b}$) reveals a decrease in fracture resistance with increasing brine volume (Fig. 5c). A linear regression against the calculated brine volumes yields a global best-fit line of $K_{IC} = -333.68\sqrt{\nu_b} + 147.73$ ($R^2 = 0.39$). This trendline is in good agreement with that established by Timco and Frederking (1983). Extrapolating this empirical trendline to a zero brine volume state yields a baseline intercept of approximately 148 kPa$\sqrt{\text{m}}$, which falls within the accepted fracture toughness range for freshwater ice (110 to 150 kPa$\sqrt{\text{m}}$) (Timco and Frederking, 1983; Schulson and Duval, 2009).

With a baseline established from natural sea ice field experiments, we now evaluate whether the age-dependent strengthening observed in the laboratory-grown ice can be explained by these thermodynamic trends. If the observed age effect was strictly governed by the liquid brine volume fraction, the laboratory data should collapse into a linear fit, much like the field specimens. However, plotting the laboratory data against $\sqrt{\nu_b}$ (Fig. 5d) yields a highly scattered distribution with a negligible coefficient of determination ($R^2 = 0.09$). Rather than following a thermodynamic trend, the data is distinctly grouped by age: at equivalent liquid brine volume fractions, older specimens exhibit higher fracture toughness values than their younger counterparts. Ultimately, this demonstrates that while brine volume influences the baseline strength, it alone cannot explain the pronounced strengthening over time observed here. This suggests that the evolving internal microstructure contributes substantially to the age-associated increase in fracture resistance.

The microstructural evolution of the laboratory-grown ice was characterized using μCT. The volumetric segmentation, summarized in Table 3, shows that the ice maintained a relatively consistent phase fraction over the 65-day interval between scans, with ice content remaining above 90% across the vertical profile. While the total porosity (air and brine) remained effectively

https://doi.org/10.5194/egusphere-2026-5861
Preprint. Discussion started: 2 November 2026
© Author(s) 2026. CC BY 4.0 License.

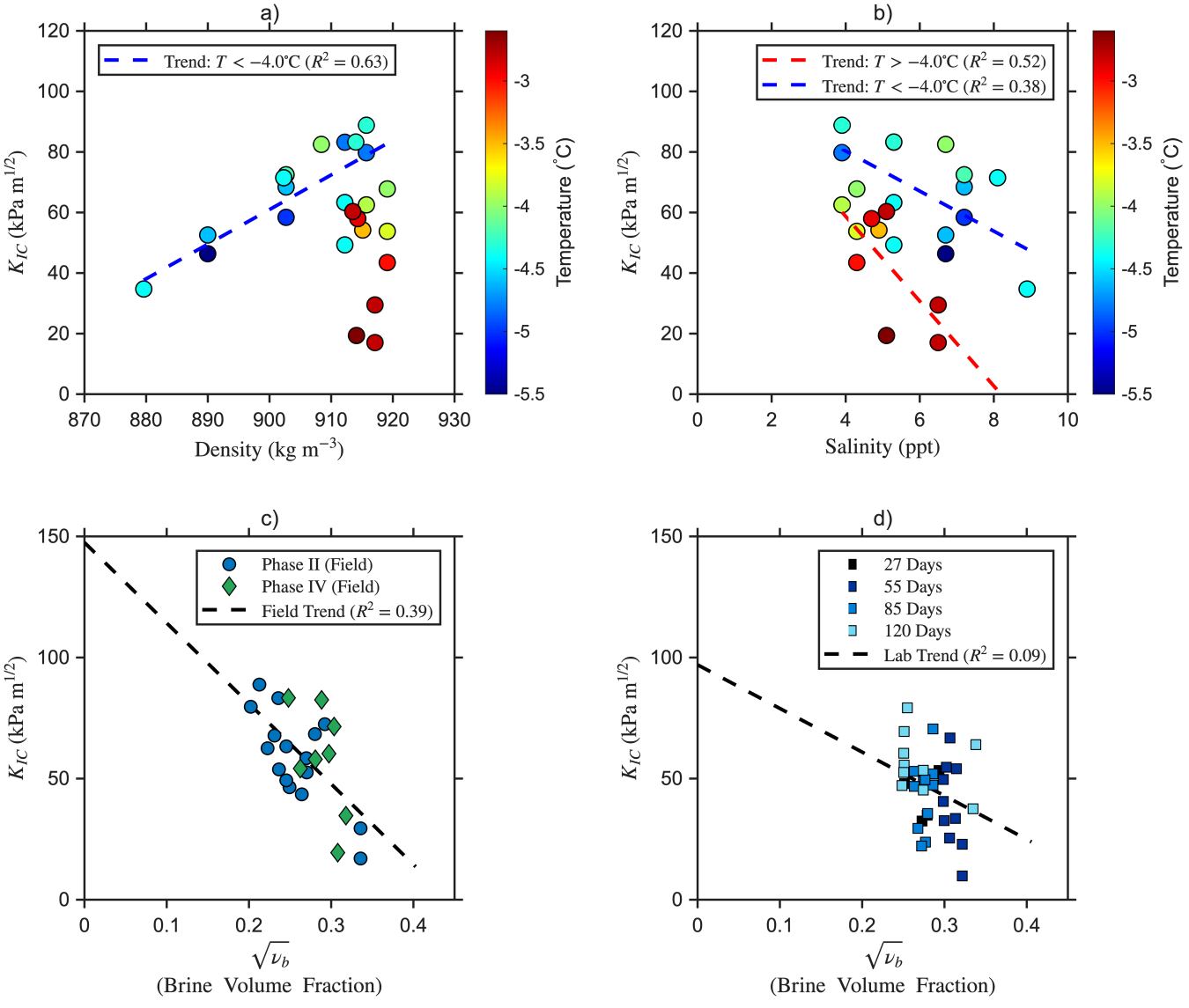
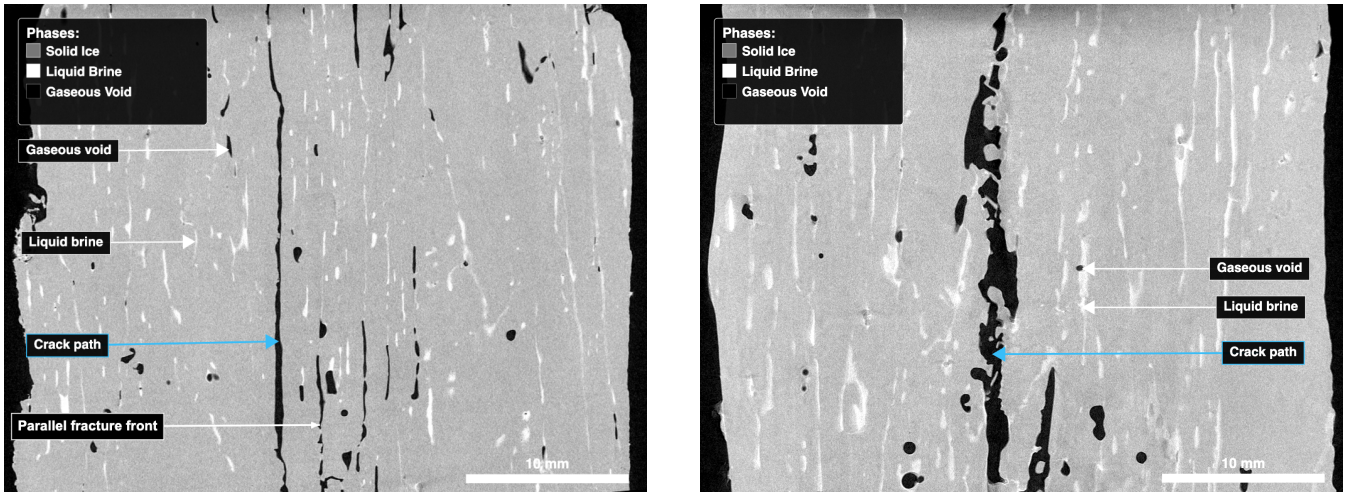


Figure 5. Fracture toughness (K_{IC}) as a function of physical state properties for natural sea ice (a–c) and laboratory-grown sea ice (d). (a) K_{IC} versus density for field specimens (Phases II (Field) and IV (Field)), featuring a linear trendline for colder ice ($T < -4.0$°C). (b) K_{IC} versus salinity for the field experiments, with linear trends identified for warmer ($T > -4.0$°C) and colder ($T < -4.0$°C) ice. For both (a) and (b), the marker colour denotes the measured ice temperature. (c) K_{IC} versus the square root of the brine volume fraction ($\sqrt{\nu_b}$) for the field specimens, derived using the Frankenstein and Garner (1967) formulation, including an overall linear trendline. (d) K_{IC} versus $\sqrt{\nu_b}$ for the laboratory-grown ice. Markers are colour-coded by age.

https://doi.org/10.5194/egusphere-2026-5861
Preprint. Discussion started: 2 November 2026
© Author(s) 2026. CC BY 4.0 License.

constant, the spatial arrangement and morphology of these phases underwent a significant transformation. To quantify this structural shift, the pore space was evaluated using three primary metrics: connectivity (the volume percentage of a phase belonging to the single largest interconnected network), shape factor (a measure of morphological complexity where a value of 1 represents a perfect sphere and higher values denote increasing complexity), and aperture (the equivalent radius of the local pore space, serving as a proxy for channel sharpness and localized stress concentration).



(a) 55-day-old ice (65 mm depth)

(b) 120-day-old ice (40 mm depth)

Figure 6. Representative reconstructed vertical cross-sections from X-ray micro-computed tomography (voxel resolution 25.0 μm) comparing the internal microstructure of (a) 55-day-old laboratory grown saline ice (depth: 65 mm) and (b) 120-day-old laboratory grown saline ice (depth: 40 mm). The three constituent phases are identified by X-ray attenuation contrast: solid ice (medium gray), liquid brine (bright white), and gaseous voids/pores including the crack (black). Call-out arrows highlight the primary crack path, a parallel fracture front (crack splinter), liquid brine drainage channels/inclusions, and gaseous air voids. The 55-day ice exhibits fine, highly dispersed vertical brine platelets, whereas the 120-day ice shows evidence of brine drainage, and enlarged vertical pore channels. Scale bars indicate 10 mm.

Between the two scans, both the connectivity and maximum aperture of the brine network increased significantly. As visually evident in Fig. 6, the younger ice is characterized by narrow, discrete inclusions, whereas the older ice develops wider, interconnected brine drainage channels. This structural evolution is quantified in Table 3. In the younger 55-day samples, brine inclusions were isolated droplets with connectivity values as low as $< 1.0\%$ in the upper layers. By 120 days, the coalescence of these pockets drove connectivity to a maximum of 73% near the surface. While the mean brine aperture remained consistent at 0.2 mm, the maximum aperture sizes and standard deviations systematically increased (e.g., maximums expanding from 0.9 mm to 1.1 mm at the 200 mm depth), indicating expansion and coalescence rather than uniform network growth. This shift is further evidenced by the brine shape factor, which increased from an average of 4.8 to 5.7. This indicates a transition from compact, discrete pockets to complex vertical channels—a conclusion supported by the orientation data, which showed a persistent dominance of the vertical growth axis in the older samples. In the air phase, mean aperture sizes in the upper

https://doi.org/10.5194/egusphere-2026-5861
Preprint. Discussion started: 2 November 2026
© Author(s) 2026. CC BY 4.0 License.

layers also expanded, growing from 0.4 mm to 0.6 mm near the surface. While this tendency for the vertical migration of brine pockets has been noted by others (e.g., Lieb-Lappen et al., 2018), the findings presented here represent the first formal three-dimensional quantification of the microstructural evolution of columnar sea ice as it ages. These observations—specifically the vertical elongation of brine inclusions, the development of a connected drainage system, and the localized expansion of brine apertures—demonstrate that our temperature and salinity controlled ice growth methodology successfully replicates the microstructural evolution previously observed in naturally aged sea ice (Lieb-Lappen et al., 2018; Cole, 2001).

Table 3. Combined µCT-derived volumetric composition, microstructural characteristics, and crack geometry. Connectivity (Conn.) indicates the volume fraction of the phase belonging to the largest interconnected cluster; Shape Factor (SF) denotes geometry (1 = sphere). Aperture is presented as mean ± standard deviation (maximum) equivalent radius, and Orient. denotes the dominant spatial orientation of the brine network. Macroscopic crack geometry is quantified by the Normalised Surface Area (A_N) of the fracture and the Mean Parallel Fronts (MPF), which indicates the degree of crack splintering.

	Air Phase				Brine Phase					Crack Geometry	
Depth (mm)	Vol. (%)	Conn. (%)	SF	Aperture: mean (max) (mm)	Vol. (%)	Conn. (%)	SF	Aperture: mean (max) (mm)	Orient.	Norm. Area (A_n)	MPF
55 Days											
25	4.6	39	2.3	0.4±0.3 (1.9)	4.6	2.6	5.0	0.2±0.07 (0.6)	Mixed	2.42	10.5
65	4.7	80	3.4	0.6±0.6 (3.7)	2.8	< 1.0	4.5	0.2±0.06 (0.5)	Vertical	3.31	18.3
200	3.4	23	1.4	0.8±0.6 (2.9)	5.6	20.0	4.8	0.2±0.08 (0.9)	Mixed	–	–
120 Days											
25	4.4	51	2.9	0.6±0.3 (1.7)	5.7	73.0	5.2	0.2±0.1 (0.8)	Mixed	1.72	5.6
40	4.1	77	2.8	0.8±0.6 (2.7)	4.7	37.0	5.4	0.2±0.09 (0.7)	Vertical	2.40	5.9
200	1.8	10	2.1	0.7±0.4 (1.9)	7.2	67.0	7.0	0.2±0.1 (1.1)	Vertical	–	–
240	2.6	32	2.4	0.7±0.4 (2.1)	6.0	60.0	5.2	0.2±0.1 (0.8)	Vertical	–	–

Furthermore, visual inspection of the fractured µCT samples suggests that propagating cracks actively route through these connected vertical brine networks—a localized failure mechanism recently observed in three dimensions by Oksala et al. (2026) and supported by foundational microstructural observations (e.g., Cole, 2001; Schulson, 2001; Schulson and Duval, 2009). Notably, this microstructural evolution affects the resulting crack geometry, which is captured by the relationship between the normalised surface area (A_N) and Mean Parallel Fronts (MPF). Specifically, A_N reflects the total fracture surface generated, while MPF quantifies the degree to which the crack splinters into overlapping parallel planes (e.g., the parallel fracture front indicated by the arrow in Fig. 6a). In the 55-day ice, the presence of small, isolated brine pockets scattered throughout the material causes the advancing fracture to splinter. This produces a high degree of parallel fracturing (average MPF = 14.4) which heavily inflates the total surface area (average $A_N = 2.87$), even though the individual splintered paths propagate along linear, direct paths (see Fig. 6). Conversely, as the ice ages to 120 days, the brine consolidates into blunted

https://doi.org/10.5194/egusphere-2026-5861
Preprint. Discussion started: 2 November 2026
© Author(s) 2026. CC BY 4.0 License.

vertical networks—evidenced by the increased aperture—separated by larger spans of continuous solid ice. Forced to weave between these consolidated blunt microstructural features, the fracture is prevented from widespread splintering (average MPF drops to 5.8). As a result, the fracture coalesces into a singular, noticeably more geometrically complex crack trajectory. Because this weaving crack front remains largely unified rather than splintering into parallel fronts, the normalised surface area decreases (average ($A_N = 2.06$), despite the heightened geometric complexity of the crack plane. Finally, it should be noted that the fracture plane was not visible in the lowermost layers of the samples (at depths ≥ 200 mm). This absence suggests that the fracture had frozen shut, a healing mechanism consistent with recent observations by Murdza et al. (2022).

While drawing definitive conclusions from two fractured specimens warrants caution, this transition toward a more localized, energy-intensive fracture path aligns well with the observed increase in pore connectivity and coalescence. This suggests a two-part explanation for the increase in fracture toughness. First, according to classical fracture mechanics (Anderson, 2017), the severity of a stress concentrator is inversely related to its root radius; as the ice ages, the widening of brine channels and air pores increases their aperture and, thus, their effective notch radius, reducing local stress concentrations through crack blunting. Second, this coalescence shifts the spatial distribution from a dense array of closely spaced, discrete pores in young ice to fewer, consolidated drainage channels separated by wide, continuous ligaments of solid ice. Rather than splintering easily through a diffuse network of flaws, the crack is forced into a more singular path through a structurally complex matrix. The combination of crack blunting and the significant mechanical energy required to fracture broad, unbroken ice ligaments likely drives the increased fracture toughness and work measured in older ice specimens, a mechanism analogous to that observed by Oksala et al. (2026).

4 Discussion

The historical discrepancy between the low fracture toughness of laboratory-grown ice and the higher values of large-scale field experiments is traditionally attributed to the scale effect (Dempsey et al., 1999). However, our results indicate that ice age must also be considered. Laboratory ice is typically tested within days or weeks of formation, yielding a young material with a highly flawed microstructure. In contrast, natural field ice undergoes prolonged thermodynamic ageing, lowering its salinity and blunting its internal flaw network. Because our data demonstrate a systematic increase in fracture resistance over 120 days, the historical lab-field discrepancy is likely not just a manifestation of the scale effect, but the compounded result of comparing young laboratory specimens to aged natural sea ice at vastly different scales.

Beyond the scale effect, the influence of loading rate must also be addressed. The experiments presented here were conducted across a wide spectrum of loading rates, ranging from load-controlled SCB tests failing in seconds to displacement-controlled ECRP tests lasting over 40 minutes. Despite these differences, the fracture toughness values aligned remarkably well at equivalent ice ages. This indicates that the observed strengthening is a genuine, age-driven material evolution rather than an experimental artifact of the loading rate. This lack of rate sensitivity aligns with recent findings by Gharamti et al. (2024), who demonstrated that rate effects in ice fracture are highly scale-dependent, remaining weak or entirely absent in specimens at or below the 0.5×1.0 m scale.

https://doi.org/10.5194/egusphere-2026-5861
Preprint. Discussion started: 2 November 2026
© Author(s) 2026. CC BY 4.0 License.

Because variables such as temperature, salinity, and thickness are intrinsically linked to age, isolating it as a strictly independent parameter is inherently challenging. However, while it is standard practice to predict mechanical strength using bulk brine volume fractions, our 120-day laboratory data illustrates that bulk porosity alone cannot explain this toughening. The µCT data provides an additional microstructural explanation: alongside total porosity, both the localized geometry (flaw radius) and spatial distribution (flaw density) of the pore space govern fracture behaviour. Two ice sheets with identical brine volumes will exhibit significantly different fracture resistances if one contains a highly interconnected array of sharp brine pockets, while the other features widely spaced, blunted drainage channels separated by ligaments of solid ice. This microstructural evolution appears to be reflected in the resulting crack geometry: the dense array of flaws in young ice facilitates a highly splintered, multi-planar fracture, whereas the consolidated structure of older ice is argued to force the crack into a more singular, localized path that requires substantially more energy to propagate.

The application of LEFM to sea ice routinely violates strict continuum assumptions, fuelling persistent scepticism regarding K_{IC} as a material property. However, its close agreement with work values and strong correlation with $\sqrt{\nu_b}$ (Timco and Frederking, 1983) validate K_{IC} as a robust engineering proxy for estimating peak loads. Furthermore, this strong time-dependence makes ice age a powerful predictive tool. While determining brine volume requires on-site core extraction and thermal profiling, age can be remotely estimated from ice charts, making it a highly practical parameter for engineering models. Although it remains unclear if K_{IC} continues to rise beyond 120 days, the work values demonstrate a clear plateau. Regardless, 120 days represents a practical upper bound for the thermodynamic ageing of seasonal first-year ice before rising spring temperatures trigger internal rotting. In the context of a warming climate, this temporal dependence has broader implications: as winter seasons shorten, the ice cover will have less time to age. Consequently, future first-year ice covers will be easier to break not only because they are thinner, but also because they are younger.

5 Conclusions

This study investigated the fracture properties of saline ice through a multi-scale experimental campaign to quantify the evolution of fracture resistance as a function of ice age. The results establish a robust physical relationship between age, fracture toughness, and internal variables:

- Laboratory-grown columnar saline ice exhibited a systematic increase in fracture toughness (K_{IC}) and work (W) over a 120-day monitoring period. This strengthening trend was consistent across varying specimen scales and geometries, and was directly validated against field experiments.
- µCT analysis revealed that as the ice ages, dense arrays of isolated brine pockets coalesce into drainage channels with expanded apertures. These observations suggest that by increasing crack-tip blunting and reducing spatial flaw density, this evolution forces crack propagation to transition from a highly splintered path to a singular, energy-intensive fracture.

https://doi.org/10.5194/egusphere-2026-5861
Preprint. Discussion started: 2 November 2026
© Author(s) 2026. CC BY 4.0 License.

- Ice age emerges as an effective metric for assessing fracture resistance. Because determining detailed microstructural properties or brine volumes requires complex on-site profiling, the strong time-dependence of K_{IC} provides a highly accessible proxy for estimating the mechanical strength of seasonal ice.
- The strong correlation between K_{IC} and work (W) supports its practical utility, aligning standard stress-intensity metrics with observed energy dissipation trends for engineering applications.

Data availability. The data supporting the findings of this study are preserved across two repositories. The micro-CT volumes and associated structural analysis results are archived through the CSC Fairdata-PAS service (https://doi.org/10.23729/fd-5faa8c8c-b1bf-349e-bf16-8d8b34bbabe4). The raw numerical data from the experiments are available via Zenodo (https://doi.org/10.5281/zenodo.23468154).

Author contributions. **Sid Oksala:** Conceptualization, methodology, experimental investigation, DIC implementation, formal data analysis and interpretation, and writing of the original manuscript. **Sakshi Devi:** Experimental investigation, DIC implementation and processing, formal data analysis and interpretation, and writing of the original manuscript. **Waqas Ahmad:** Experimental investigation, DIC implementation and analysis, and data interpretation. **Jukka Kuva:** Micro-CT scanning methodology, formal analysis of CT data, manuscript review and editing. **Jukka Tuhkuri:** Conceptualization, methodology, data interpretation, manuscript review and editing, and supervision.

Competing interests. The authors declare that they have no conflict of interest.

Acknowledgements. The financial support by the Research Council of Finland, through the project Fracture of Ice, decision number 351229, is gratefully acknowledged. This research was also funded in part by the COLDHUB project, supported by Nordforsk, and the Research Council of Norway. Additional financial support was provided by the Jenny and Antti Wihuri Foundation and the Maritime Foundation (Merenkulunsäätiö). X-ray tomography was funded by the Research Council of Finland via the RAMI infrastructure grant (#293109). Finally, the authors thank Knut Høyland, the University Centre in Svalbard (UNIS), and the participants of Course AT311 for facilitating the field work and providing essential logistical support.

https://doi.org/10.5194/egusphere-2026-5861
Preprint. Discussion started: 2 November 2026
© Author(s) 2026. CC BY 4.0 License.

References

Adamson, R., Shapiro, L., and Dempsey, J.: Core-based SCB fracture of aligned first-year sea ice (phases III and IV), Journal of cold regions engineering, 11, 30–44, https://doi.org/10.1061/(asce)0887-381x(1997)11:1(30), 1997.

Ahmad, W.: Understanding ice fracture using Digital Image Correlation-From microstructural crack arrest to comparison with the visco-elastic fictitious crack model, Aalto University, https://aaltodoc.aalto.fi/items/92a28357-0aa1-4290-88b1-dcd77224f5c0, 2024.

Anderson, T. L.: Fracture Mechanics: Fundamentals and Applications, CRC press, 4th edn., https://doi.org/10.1201/9781315370293, 2017.

Cole, D. M.: The microstructure of ice and its influence on mechanical properties, Engineering Fracture Mechanics, 68, 1797–1822, https://doi.org/10.1016/S0013-7944(01)00031-5, 2001.

Cole, D. M. and Shapiro, L. H.: Observations of brine drainage networks and microstructure of first-year sea ice, Journal of Geophysical Research: Oceans, 103, 21 739–21 750, https://doi.org/10.1029/98JC01264, 1998.

Dempsey, J. and Mu, Z.: Weight function for an edge-cracked rectangular plate, Engineering Fracture Mechanics, 132, 93–103, https://doi.org/https://doi.org/10.1016/j.engfracmech.2014.10.023, 2014.

Dempsey, J., Adamson, R., and Mulmule, S.: Scale effects on the in-situ tensile strength and fracture of ice. Part II: First-year sea ice at Resolute, NWT, International journal of fracture, 95, 347–366, https://doi.org/10.1023/a:1018650303385, 1999.

Dempsey, J. P.: The fracture toughness of ice, in: Ice-Structure Interaction: IUTAM/IAHR Symposium St. John's, Newfoundland Canada 1989, pp. 109–145, Springer, https://doi.org/10.1007/978-3-642-84100-2_8, 1991.

Dempsey, J. P., Cole, D. M., and Wang, S.: Tensile fracture of a single crack in first-year sea ice, Philosophical Transactions of the Royal Society A: Mathematical, Physical and Engineering Sciences, 376, 20170 346, https://doi.org/10.1098/rsta.2017.0346, 2018.

Devi, S., Oksala, S., Ahmad, W., and Tuhkuri, J.: Fracture Behaviour of Saline Ice: DIC-Measured Crack Growth and J-Integral Analysis, in: Proceedings of the 28th IAHR International Symposium on Ice, Shanghai, China, https://www.iahr.org/library/infor?pid=40973, 2026.

Domander, R., Felder, A. A., and Doube, M.: BoneJ2 - refactoring established research software, Wellcome Open Research, 6, 37, https://doi.org/10.12688/wellcomeopenres.16619.2, 2021.

Frankenstein, G. and Garner, R.: Equations for determining the brine volume of sea ice from- 0.5° to- 22.9° C., Journal of Glaciology, 6, 943–944, https://doi.org/10.3189/s0022143000020244, 1967.

Gharamti, I., Ahmad, W., Puolakka, O., and Tuhkuri, J.: Thickness-independent fracture in columnar freshwater ice: An experimental study, Engineering Fracture Mechanics, 298, 109 906, https://doi.org/https://doi.org/10.1016/j.engfracmech.2024.109906, 2024.

Kuruppu, M. D., Obara, Y., Ayatollahi, M. R., Chong, K., and Funatsu, T.: ISRM-suggested method for determining the mode I static fracture toughness using semi-circular bend specimen, Rock Mechanics and Rock Engineering, 47, 267–274, https://doi.org/10.1007/s00603-013-0422-7, 2014.

LeClair, E., Adamson, R., and Dempsey, J.: Core-based SCB fracture of aligned first-year sea ice (Phase VI), Journal of cold regions engineering, 11, 45–58, https://doi.org/10.1061/(asce)0887-381x(1997)11:1(45), 1997.

Lieb-Lappen, R. M., Kumar, D. D., Pauls, S. D., and Obbard, R. W.: A network model for characterizing brine channels in sea ice, The Cryosphere, 12, 1013–1018, https://doi.org/10.5194/tc-12-1013-2018, 2018.

Murdza, A., Schulson, E. M., Renshaw, C. E., and Polojärvi, A.: Rapid healing of thermal cracks in ice, Geophysical Research Letters, 49, e2022GL099 771, https://doi.org/10.1029/2022GL099771, 2022.

https://doi.org/10.5194/egusphere-2026-5861
Preprint. Discussion started: 2 November 2026
© Author(s) 2026. CC BY 4.0 License.



Nansen, F. and Sverdrup, O. N.: Farthest North; being the record of a voyage of exploration of the ship "Fram" 1893-96, and of a fifteen months' sleigh journey by Dr. Nansen and Lieut. Johansen, vol. 1, Harper & Brothers, New York, https://archive.org/details/farthestnorthbei01nans/page/n7/mode/2up, 1897.

Oksala, S., Puolakka, O., Izadi, M., and Tuhkuri, J.: Salinity-controlled laboratory production of ice, in: International Association for Hydro-Environment Engineering and Research International Symposium on Ice, International Association for Hydro-Environment Engineering and Research, https://www.iahr.org/library/infor?pid=30379, 2024.

Oksala, S., Lehto, P., and Tuhkuri, J.: A Practical Method to Establish the Apparent Fracture Toughness of Ice in the Field, in: Proceedings of the 28th International Conference on Port and Ocean Engineering under Arctic Conditions, Port and Ocean Engineering under Arctic Conditions, https://research.aalto.fi/en/publications/a-practical-method-to-establish-the-apparent-fracture-toughness-o/, 2025.

Oksala, S., Maus, S., Lu, W., and Tuhkuri, J.: Three-dimensional geometry of tensile fracture in columnar saline ice, Journal of the Mechanics and Physics of Solids, under review, 2026.

Pearce, E., Marsh, O. J., Mitchell, T. M., Tuhkuri, J., Thomas, E. R., and Johnson, S.: Impact of surface melt and brine infiltration on fracture toughness of ice shelves, EGUsphere, 2025, 1–19, https://doi.org/10.5194/tc-20-2723-2026, 2025.

Rist, M. A., Sammonds, P. R., Murrell, S. A. F., Meredith, P. G., Oerter, H., and Doake, C. S. M.: Experimental fracture and mechanical properties of Antarctic ice: preliminary results, Annals of Glaciology, 23, 284–289, https://doi.org/10.3189/s0260305500013550, 1996.

Schulson, E. M.: Brittle failure of ice, Engineering Fracture Mechanics, 68, 1839–1887, https://doi.org/10.1016/S0013-7944(01)00037-6, 2001.

Schulson, E. M. and Duval, P.: Creep and Fracture of Ice, Cambridge University Press, Cambridge, ISBN 9780521806206, https://doi.org/10.1017/CBO9780511581397, 2009.

Smith, R. A.: The application of fracture mechanics to the problem of crevasse penetration, Journal of Glaciology, 17, 223–228, https://doi.org/10.3189/s0022143000013563, 1976.

Timco, G. W. and Frederking, R. M. W.: Flexural strength and fracture toughness of sea ice, Cold Regions Science and Technology, 8, 45–60, https://doi.org/10.1016/0165-232x(83)90015-0, 1983.

Weeks, W.: On Sea Ice, University of Alaska Press, Fairbanks, AK, ISBN 978-1-60223-079-8, https://upcolorado.com/university-of-alaska-press/on-sea-ice, 2010.